LAWRENCE
LIVERMORE
NATIONAL
LABORATORY

LLNL-JRNL-621592

Onset of Hydrodynamic Mix in High-Velocity, Highly Compressed Inertial Confinement Fusion Implosions

T. Ma, S. V. Weber, N. Izumi, P. T. Springer, P. K. Patel, M. H. Key, L. J. Atherton, L. R. Benedetti, D. K. Bradley, D. A. Callahan, P. M. Celliers, C. J. Crejan, E. L. Dewald, S. N. Dixit, T. Doeppner, D. H. Edgell, S. Glenn, G. Grim, S. W. Haan, B. A. Hammel, D. Hicks, W. W. Hsing, O. S. Jones, S. F. Khan, J. D. Kilkenny, J. L. Kline, G. A. Kyrala, O. L. Landen, S. LePape, B. J. MacGowan, A. J. Mackinnon, A. G. MacPhee, N. B. Meezan, J. D. Moody, A. Pak, T. Parham, H. S. Park, J. E. Ralph, S. E. Regan, B. A. Remington, H. F. Robey, J. S. Ross, B. K. Spears, V. Smalyuk, L. J. Suter, R. Tommasini, R. P. Town, J. D. Lindl, M. J. Edwards, S. H. Glenzer, E. I. Moses

February 25, 2013

Physical Review Letters

Disclaimer

Onset of Hydrodynamic Mix in High-Velocity, Highly Compressed Inertial Confinement Fusion Implosions

T. Ma,[1] P. K. Patel,[1] N. Izumi,[1] P. T. Springer,[1] M. H. Key,[1] L. J. Atherton,[1] L. R. Benedetti,[1] D. K. Bradley,[1] D. A. Callahan,[1] P. M. Celliers,[1] C. J. Cerjan,[1] D. S. Clark,[1] E. L. Dewald,[1] S. N. Dixit,[1] T. Döppner,[1] D. H. Edgell,[2] R. Epstein,[2] S. Glenn,[1] G. Grim,[3] S. W. Haan,[1] B. A. Hammel,[1] D. Hicks,[1] W. W. Hsing,[1] O. S. Jones,[1] S. F. Khan,[1] J. D. Kilkenny,[4] J. L. Kline,[3] G. A. Kyrala,[3] O. L. Landen,[1] S. Le Pape,[1] B. J. MacGowan,[1] A. J. Mackinnon,[1] A. G. MacPhee,[1] N. B. Meezan,[1] J. D. Moody,[1] A. Pak,[1] T. Parham,[1] H.-S. Park,[1] J. E. Ralph,[1] S. P. Regan,[2] B. A. Remington,[1] H. F. Robey,[1] J. S. Ross,[1] B. K. Spears,[1] V. Smalyuk,[1] L. J. Suter,[1] R. Tommasini,[1] R. P. Town,[1] S. V. Weber,[1] J. D. Lindl,[1] M. J. Edwards,[1] S. H. Glenzer,[1] and E. I. Moses[1]

[1] *Lawrence Livermore National Laboratory, Livermore, California 94550, USA*
[2] *Laboratory for Laser Energetics, University of Rochester, Rochester, New York 14623, USA*
[3] *Los Alamos National Laboratory, Los Alamos, New Mexico 87545, USA*
[4] *General Atomics, San Diego, California, USA*

(Dated: February 19, 2013)

Deuterium-tritium inertial confinement fusion implosion experiments on the National Ignition Facility have demonstrated yields ranging from $0.8–7\times10^{14}$, and record fuel areal densities of 0.7–1.3 g/cm^2. These implosions use hohlraums irradiated with shaped laser pulses of 1.5–1.9 MJ energy. The laser peak power, and duration at peak power were varied, as were the capsule ablator dopant concentrations and shell thicknesses. We quantify the level of hydrodynamic instability mix of the ablator into the hot spot from the measured elevated absolute x-ray emission of the hot spot. We observe that DT neutron yield and ion temperature decrease abruptly as hot spot mix mass increases above ∼200 ng. The comparison with radiation-hydrodynamic modeling indicates that low mode asymmetries and increased ablator surface perturbations may be responsible for the current performance.

PACS numbers: 52.57.-z, 52.57.Fg, 87.59.-e

Current inertial confinement fusion (ICF) experiments [1, 2] conducted on the National Ignition Facility (NIF) [3] seek to indirectly drive a spherical implosion to ignite deuterium-tritium fuel. In this scheme, lasers irradiate the inner wall of a high-Z hohlraum, producing a soft x-ray drive with a Planckian spectrum of 300 eV temperature that ablates and compresses the fuel capsule. Ignition and high fusion yield > 1 MJ will occur when the thermonuclear fuel is assembled in a low adiabat, high convergence implosion to high areal density ($\rho R > 1.4$ g/cm^2) enclosing a central hot spot of temperature > 4 keV and $\rho R > 0.3$ g/cm^2. At this stage, alpha deposition further heats the hot spot and generates a self-sustaining burn wave that is launched into the fuel [4–6]. The strategy to achieve these conditions for ignition is outlined in a series of articles by Edwards, Landen, Haan, *et al.*, [2, 7, 8].

The implosions employ a tailored laser pulse with a sequence of four distinct steps, producing four shocks that successively merge until all coalesce just inside the inner radius of the ice. With each shock merger, compression and the shock velocity are both increased. The ablation pressure following the fourth shock accelerates the shell inwards, to reach a peak velocity of 370 km/s.

Hydrodynamic instabilities, such as the Rayleigh-Taylor (RT), Richtmyer-Meshkov (RM), and Kelvin-Helmoltz (KH) instabilities can degrade ICF capsule performance. These instabilities have been studied extensively in direct drive and indirect drive, and in a variety of geometries; much of the large body of work is reviewed in [9, 10]. The evolution of instabilities is sensitive to ablation rate and surface characteristics [11], with the dominant concern for ICF being ablation-front RT [12]. For ignition experiments, the tradeoff is between implosion velocity, which continues to increase as more mass is ablated, and the penetration of ablator material into the fuel by outer surface imperfections that grow at the ablation front due to the RT instability [13, 14]. This growth can also seed perturbations at the fuel-ablator interface, which in turn become RT unstable during deceleration and stagnation. In situations with large RT growth, the ablator may mix into the DT fuel layer and hot spot, increasing the radiative cooling and degrading performance.

In this letter, we present a series of experiments conducted at the NIF that show the sensitivity of performance to the level of ablator-hot spot mix. We have developed a simple model that infers the level of DT hot spot contamination from higher Z ablator material by the presence of excess absolute x-ray emission from the hot spot. The ratio of the measured x-ray emission to the calculated emission based on the 14.1 MeV neutron yield and the hot spot temperature is an indication of carbon mixed into the compressed core. The DT yield and ion temperature decrease nearly monotonically with increasing levels of mix mass. By incorporating artificially

enhanced mix, or low mode asymmetries and increased surface perturbations, 2D radiation-hydrodynamic simulations are approaching the experimental results.

Figure 1 illustrates an ignition hohlraum heated by 192 laser beams with typical laser pulse shapes shown where peak power and drive duration are varied. The lasers deliver a total energy of 1.5–1.9 MJ, with peak power ranging from 320–450 TW, at a wavelength of 351 nm. The targets were of the nominal Rev 5 ignition design [8] using equimolar mixtures of DT cryogenically prepared as a solid 69 μm-thick ice layer with a fuel mass of 170 μg encircling a DT gas mass of 1 μg, all encased in a plastic (CH) shell. This CH ablator was of a thickness of 195 μm (T0) or 215 μm (T1), and was doped with trace amounts of silicon, germanium, or copper, with an outside diameter of 2.26 mm. Implosions were carried out using both gold and depleted uranium (DU) hohlraums, of either 5.44 or 5.75 mm diameter. A sample of several of the pulse shapes are shown with varying peak power and duration of the fourth pulse. For a subset of the implosions, an extended drive (such as the 320 TW pulse shape in Fig. 1) lengthened the duration of the fourth pulse to within 1 ns of bangtime (peak compression).

At stagnation, the hot spot reaches temperatures of several keV, and emits ~100 J of x-rays, the spectral and spatial variation of which contains key information that we use to evaluate the implosion performance. The bulk of the x-ray emission above 6 keV observed is combined recombination and bremsstrahlung continuum [5]. Any ablator material that is mixed into the compressed fuel will equilibrate with the hot spot, and as the ablator is primarily composed of higher Z CH, will radiatively cool the hot spot, reducing the ion temperature and decreasing the neutron yield.

The model quantifies the ablator mix into the hot spot by determining the individual contributions of DT and CH to the radiated free-free and free-bound emission. The total neutron yield Y_{DT} from the fusion reaction D+T $\rightarrow$ ^{4}He (3.5 MeV) + n (14.1 MeV) is given by:

$$\begin{aligned} Y_{DT} &= n_D n_T \left\langle \sigma_{DT} v(T_i) \right\rangle V \Delta t, \\ &= f_D f_T \frac{A_v^2}{\bar{A}^2} \rho_{DT}^2 \left\langle \sigma_{DT} v(T_i) \right\rangle V \Delta t, \end{aligned} \tag{1}$$

where n_D and n_T are the number densities of deuterium and tritium ions, respectively, and f_D and f_T their corresponding atomic fractions; A_v is Avogadro's number; $\bar{A}$ is the mean atomic mass; ρ_{DT} is the density; $\langle \sigma_{DT} v(T_i) \rangle$ is the DT reactivity cross-section at the ion temperature T_i; V is the hot spot volume; and Δt the burn duration.

The x-ray emission from the hot spot in the optically thin limit can be written as

$$\begin{aligned} X_\nu = 4\pi\, j_{DT} \times (1 + \sum x_i Z_i)\big(1 + \sum x_i \frac{j_i}{j_{DT}}\big) \\ \times e^{-\tau_\nu^{shell}} \times V \Delta t \ \ (\mathrm{erg/Hz}), \end{aligned} \tag{2}$$

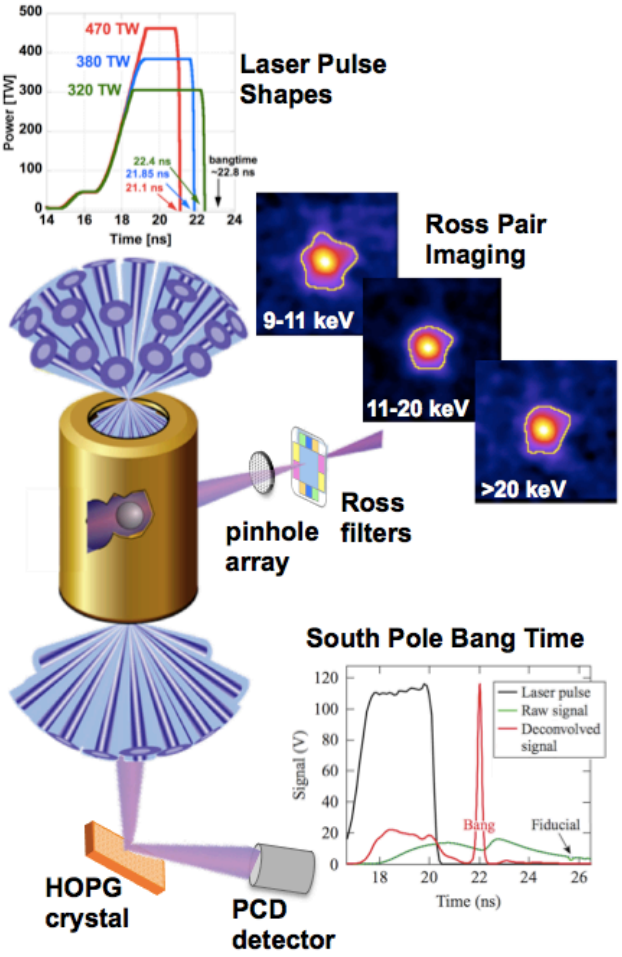

FIG. 1. Schematic of an ignition target with an example of the laser pulseshapes used, where peak power and duration of the fourth pulse is varied. Viewing the implosion through a diagnostic patch in the hohlraum, the Ross filters [15, 16] employ a pinhole array projecting through five different filter materials to image the temperature- and density-sensitive x-ray emission. The South Pole Bang Time diagnostic [17, 18] views the implosion through the lower hohlraum laser entrance hole.

where j_{DT} is the total DT emissivity (see Eq. 3); j_i is the total emissivity of ion i; the term $(1 + \sum x_i Z_i)(1 + \sum x_i \frac{j_i}{j_{DT}})$ represents the enhancement in emission due to mix of ions with atomic number Z_i, and fraction x_i of the total number of D + T atoms; and τ_ν^{shell} is the optical depth of the shell [5, 19]. The free-free continuum emission scales as Z^2, while free-bound emission scales as Z^4. Thus for CH mix, the radiative recombination contribution becomes a significant enhancement factor that cannot be overlooked.

The DT emission coefficients are obtained from Kirchoff's law and a fit to the OPAL [20] and DCA [21]

opacity tables:

$$j_{DT} = \alpha_\nu B_\nu(T_e) \simeq \frac{\rho_{DT}^2}{A^2} \frac{e^{-h\nu/kT_e}}{(h\nu)^{0.33}} \text{ (erg/s/cm}^3\text{/sr/Hz)}, \quad (3)$$

where α_ν is the absorption coefficient; $B_\nu(T_e)$ is the Planck function; and $h\nu$ is the photon energy in units of keV. The ratio of the x-ray to neutron yield is then independent of the hot spot density, volume, and burn width, and scales only with temperature, shell attenuation, and mix fraction:

$$\frac{X_\nu}{Y_{DT}} \simeq \frac{4\pi}{f_D f_T A_v^2 \langle \sigma_{DT} v(T_i) \rangle} \frac{e^{-h\nu/kT_e}}{(h\nu)^{0.33}} \times (1 + \sum x_i Z_i)(1 + \sum x_i \frac{j_i}{j_{DT}}) \times e^{-\tau_\nu^{shell}} \text{(erg/Hz)}. \quad (4)$$

The neutron yield and ion temperature are measured by a suite of neutron time-of-flight (NTOF) detectors [22], neutron activation diagnostics [23], and the magnetic recoil spectrometer [24]. The absolute x-ray emission from the hot spot is measured by two diagnostics: the Ross Pair Imager and South Pole Bang Time (SPBT). The Ross Pair diagnostic [15, 16] employs differential filtering [25] to provide time-integrated, absolute x-ray self-emission images of the imploded core in five energy channels starting at 6 keV and above. The simplifying assumptions underlying Eq. 4 are that the nuclear and x-ray emission volumes and burn durations are the same, $T_e = T_i$, and that the ablator material mixed into the hot spot is uniformly distributed. Then, using the measured values of Y_{DT} and T_i, we use Eq. 4 to calculate the unattenuated x-ray emission spectrum from a clean DT hot spot. This spectrum is convolved with the filter transmission of each Ross channel and the image plate detector response. The best fit values for the shell optical depth, τ_ν^{shell}, and the $(1 + \sum x_i Z_i)(1 + \sum x_i \frac{j_i}{j_{DT}})$ enhancement factor are then found by the reduced χ-squared minimization method. In the case of CH mix, $Z_C = 6$, $Z_H = 1$, and we obtain $x \equiv x_C = x_H$. The CH mix mass is then given by

$$mass_{CH} = \frac{x(A_C + A_H)}{A_{DT}} mass_{DT} = x\frac{13}{2.5} mass_{DT} \quad (5)$$

using the DT hot spot mass calculated from Eq. 1. Typical calculated hot spot masses for the set of DT implosions were 3.8 ± 1.5 μg. Systematic uncertainty in the absolute response of the x-ray detector is removed by normalizing to the cleanest shot, setting it to have a nominal mix mass of ∼ 30 ng. While this method has a large uncertainty for low mix shots (mix mass $\lesssim$ 150 ng), the uncertainty decreases with increasing mix.

The SPBT diagnostic records the absolute temporally-resolved x-ray emission in a narrow band at 10.85 ± 0.3 keV [17, 18]. When corrected for shell attenuation (by using the optical depth derived from the Ross Pairs, or estimated using the initial ablator composition and remaining mass inferred from equivalent convergent ablator experiments [26]), the absolute SPBT signal gives an additional measurement of the x-ray to neutron yield ratio and, hence, using the same method as before, the CH mix mass. The mix mass measured by the two diagnostics are in good agreement with each other and the mean value is reported.

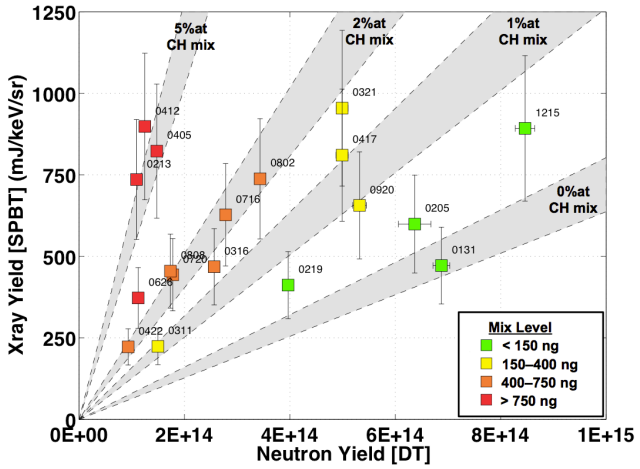

FIG. 2. X-ray yield (as measured by SPBT) versus neutron yield for the set of layered NIF implosions. Gray bands show percentages of atomic CH mix into the clean DT over the range of ion temperatures of 1.7–3.9 keV represented by this set of shots.

Figure 2 plots the measured 10.85 keV hot spot x-ray yield from the SPBT diagnostic, corrected for shell attenuation, versus the measured DT neutron yield for the layered implosions performed on the NIF. The gray bands are the theoretical x-ray to neutron yield ratios from Eq. 4 for a clean hot spot and mix ratios of $x = 1\%$, 2%, and 5% atomic mix from the ablator into the hot spot. The width of each band represents the calculations spanning the ion temperature range $1.7 < T_i < 3.9$ keV, and indicates the relatively weak dependence of the ratio on temperature. The shots exhibit a wide variation in mix from relatively clean to 5% atomic CH, which corresponds to several micrograms of CH in the hot spot.

Figure 3 shows the observed DT neutron yield versus the inferred mix mass for the database of cryogenic DT implosions completed on NIF. We observe the highest Y_n for shots with mix masses of below 200 ng of mix, and yield performance dropping steeply just beyond that. Details of each shot, such as differences in peak laser powers and fourth pulse slope, fourth pulse duration, and pulse shapes, hohlraum materials, capsule dopant concentrations, and capsule surface defects, influence the actual measured level of mix and account for the scatter in the data set. As shown, the bulk of our shots have employed

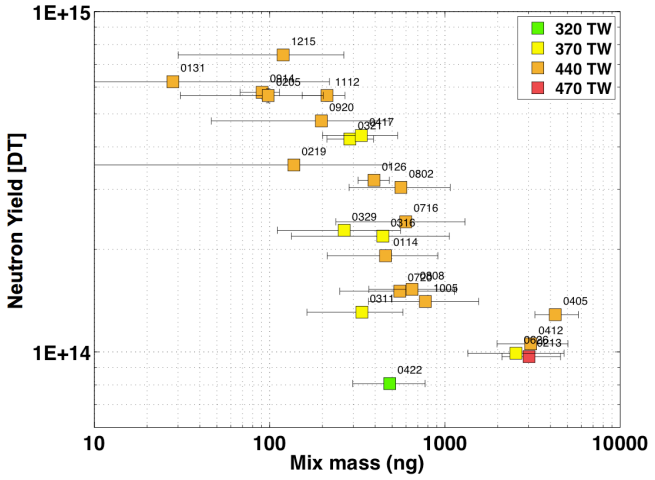

FIG. 3. DT 14.1 MeV neutron yield plotted against the inferred mix mass for the full array of layered NIF implosions. Points are color coded by peak laser power. When DU hohlraums are used, the effective peak power is increased by 25 TW (accounted for here) due to the increased x-ray conversion efficiency as compared to gold hohlraums [27]. The onset of the mix "cliff" at ∼200 ng is apparent in the accompanying reduction of yield.

peak powers of 370–440 TW, over which we observe large variability in the amount of measured mix, with some shots showing significant performance degradation due to high mix. We also did a low power shot of 320 TW and a high power shot of 470 TW (pulse shapes shown in Fig. 1). Both implosions showed substantial mix. It is possible that the expected decreased classical growth due to lower acceleration with the lower power shot was not enough to overcome the decreased ablative stabilization. In the case of the high peak power shot, likely the increased x-ray drive resulted in a thinner ablator during the acceleration phase, increasing susceptibility to instability feedthrough. Simulations of these shots are exploring the plausibility of these hypotheses. We have also examined the yield versus mix mass trend for correlations across a large number of other shot attributes and in most cases find only weak trends. One persistent trend is that only shots with a truncated fourth pulse and nominal Si dopant levels in the ablator (1xSi) lie in the low mix region. These pulses reduce the late time acceleration of the shell and allow it to decompress, reducing ablation front growth rates and the level of instability feedthrough.

Figure 4 plots the experimentally measured DT neutron yield against T_i for the ensemble of layered shots. It shows that the reduction in T_i as the yield decreases is more gradual than predicted by the $Y_{DT} \sim T_i^{4.7}$ theoretical scaling for the 1D neutron yield in the absence of alpha deposition [28]. This slower scaling is consistent with assuming the stagnated DT pressure $\sim nT_i$ is conserved for small amounts of mix, such that $Y_{DT} \sim n^2 T_i^{4.7}$ is then $\sim T_i^{2.7}$. Simulations that are perfectly spherical and have no mix dramatically over-estimate the yield in these implosions, while giving an ion temperature that is comparable to the upper limit of what is observed in the various shots. Post-shot 2D radiation hydrodynamic HYDRA [29] simulations, using our current knowledge of drive asymmetries, capsule surface roughness, ice surface roughness, and approximations for the effect of the fill tube (used to fill the capsule with cryogenic DT fuel) and capsule support tent, typically predict DT neutron yields that are higher than experimentally observed by factors of 5–10 [30]. However, the data trend is reproduced when artificially enhanced mix is included in simulations, as is seen by the gray hatched crosses that represent 30, 300, and 3000 ng of CH preloaded into the DT gas. While the simulations still overpredict the yield as compared to the data, we can recover the correct slope, demonstrating that radiative cooling through mix plays a significant role in explaining the performance.

To account for uncertainties in simulations of the RT instability, we have performed calculations with the initial surface perturbations arbitrarily increased until the yield is similar to observed. These simulations show reasonable agreement with the observed low-mix yield and ion temperature. The two indicated simulations with 5× surface roughness (open crosses in Fig. 4) differ in assumed detailed shape of the initial roughness. These simulations also agree with the observed areal density, and with the sizes of the x-ray and neutron images. These simulations do not bring any CH mix into the hot spot.

Further, modeling in which low mode perturbations are applied (solid purple crosses in Fig. 4) also tend to bring the simulations closer to the experimental data [31]. These simulations impose a radiation drive with a P_1 Legendre mode asymmetry of 0.5, 1, and 2%, which progressively decrease the yield, while incrementally increasing the T_i. These drive asymmetries result in a heavily disturbed cold fuel, with the hot spot displaced, reducing the central pressure. As P_1 is difficult to diagnose experimentally (requiring absolute knowledge of hot spot location relative to hohlraum or radiation drive), a P_1 asymmetry may appear as a P_2 or P_3 in images of the neutrons or x-ray self-emission (which originate from the low pressure region). Attempting to correct for P_2 and P_3 in the hot spot could further reduce yield by 2×. Other recent simulation results investigating large amplitude P_4 asymmetries [32] also result in significant yield reduction, while large mid-mode asymmetries are found to generate a strong vorticity, which can lead to turbulent mixing of the cold fuel and ablator into the hot spot [33].

Imaging of the hot spot emission from the equator and the pole with gated x-ray framing cameras show that these 3D low-mode asymmetries can be significant (see Fig. 1), and recent backlit radiography of the in-flight shell show even more pronounced shape and ρR asymme-

tries. A statistical mix analysis shows that if significant regions of the shell are 5-10 μm thinner than the average, ablator mix into the hot spot can increase by factors of several, which in turn could decrease the predicted yield by factors of several.

A full understanding of the question of mix and its effects on performance will likely require a suite of reasonably resolved 3D simulations, including both surface perturbations and the observed low-mode asymmetries. Incorporating high levels of mix into the simulations is ongoing work, as is quantifying the connection between the simulated Rayleigh-Taylor growth, the known deviations from sphericity, and the rather high levels of perturbations required to match the observed yields.

A number of mix mitigation techniques are presently being pursued, including reducing the seeds for RT growth by fabricating smoother capsules, and modifying the capsule design, possibly with thicker ice and thicker ablators. In addition, laser pulse shape tuning to increase the strength of the initial shock is expected to provide increased RT ablative stabilization. This, however, comes with a tradeoff of raising the adiabat of the target due to the increased shock heating and lowers the final fuel pressure. Effects of the intrinsic perturbation introduced by the capsule support tent and other large scale nonuniformities are also being investigated.

It should be noted that the estimates of mix mass using the method described in this paper are lower bound estimates due to the assumption of homogeneous mix of the CH within the hot spot, heating the injected material to the same electron temperature as the core. In reality, perturbation growth of surface defects can produce a jet of ablator material that introduces mass into the hot spot [34]. The jet region, which may be composed of as much as several hundred ng of CH, would be denser and colder than the hot spot, and would not radiate as brightly. Nonetheless, our measurements showing the onset of the mix cliff at several hundred nano grams of mix agrees with the estimates in our point design [8]. For smaller amounts of hot spot mix (<100 ng), spectroscopy of line emission from higher-Z dopants in specific layers of the ablator [8] has been demonstrated to be a sensitive quantitative measurement of mix of ablator into the hot spot [35]. Spatially and temporally resolving where and when the hot spot mix occurs is also a current focus of the ignition campaign.

In summary, we have developed a model that uses the ratio of the experimentally measured level of elevated absolute x-ray emission to neutron yield to quantify the impurity mix of shell ablator into the hot spot. Applying this model to the full ensemble of indirect-drive National Ignition Facility DT cryogenically layered implosions to date has defined a "mix cliff" of performance degradation above several hundred nano grams of mix mass, consistent with expected sensitivity to mix mass. The high velocity, high convergence conditions demonstrated have resulted in increased hydrodynamic mix of the ablator into the hot spot. Simulations with increased surface roughness or imposed low mode asymmetries can bring the predicted yields and ion temperatures close to agreement with experimental observations.

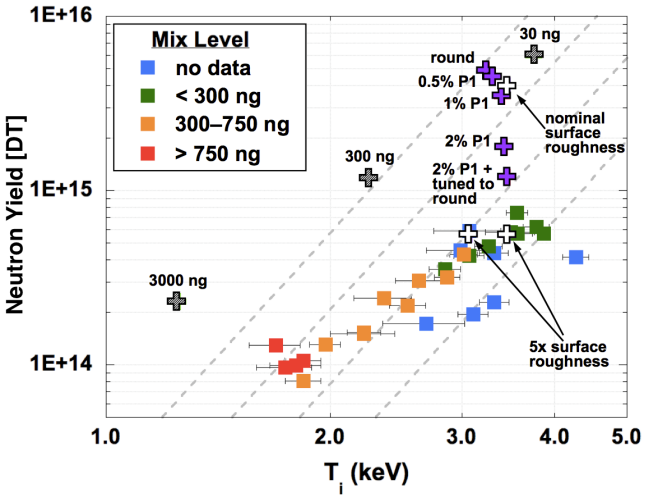

FIG. 4. Experimental DT neutron yield versus T_i (solid square symbols) distinguished by level of mix mass. Dashed lines represent the expected $Y \sim T_i^{4.7}$ power scaling [28] for constant hot spot densities. Open crosses are 2-D HYDRA simulations for a 370 TW drive with surface roughness increased to match yield and T_i. Filled (purple) crosses are a set of simulations that vary the P1 low mode asymmetry. Hatched (gray) crosses are simulations that include artificially enhanced mix.

We wish to thank the NIF operations team. This work was performed under the auspices of the U.S. Department of Energy by Lawrence Livermore National Laboratory under Contract DE-AC52-07NA27344.

[1] S. H. Glenzer, D. A. Callahan, A. J. Mackinnon, J. L. Kline, G. Grim, E. T. Alger, R. L. Berger, L. A. Bernstein, R. Betti, D. L. Bleuel, et al., Physics Of Plasmas **19**, 056318 (2012).
[2] M. J. Edwards, J. D. Lindl, B. K. Spears, S. V. Weber, L. J. Atherton, D. L. Bleuel, D. K. Bradley, D. A. Callahan, C. J. Cerjan, D. Clark, et al., Physics Of Plasmas **18**, 051003 (2011).
[3] G. H. Miller, E. I. Moses, and C. R. Wuest, Nuclear Fusion **44**, S228 (2004).
[4] J. Nuckolls, L. Wood, A. Thiessen, and G. B. Zimmerman, Nature **239**, 139 (1972).
[5] S. Atzeni and J. Meyer-Ter-Vehn, *The Physics of Inertial Fusion* (Oxford Science, 2004).
[6] B. K. Spears, S. Glenzer, M. J. Edwards, S. Brandon, D. Clark, R. Town, C. Cerjan, R. Dylla-Spears, E. Mapoles, D. Munro, et al., Physics Of Plasmas **19**, 6316 (2012).
[7] O. L. Landen, J. Edwards, S. W. Haan, H. F. Robey,

J. Milovich, B. K. Spears, S. V. Weber, D. S. Clark, J. D. Lindl, B. J. Macgowan, et al., Physics Of Plasmas **18**, 051002 (2011).

[8] S. W. Haan, J. D. Lindl, D. A. Callahan, D. S. Clark, J. D. Salmonson, B. A. Hammel, L. J. Atherton, R. C. Cook, M. J. Edwards, S. Glenzer, et al., Physics Of Plasmas **18**, 051001 (2011).

[9] J. Lindl, P. Amendt, R. Berger, and S. Glendinning, Physics Of Plasmas (2004).

[10] N. M. Hoffman, *Hydrodynamic instabilities in inertial confinement fusion. In M. B. Hooper, editor, Laser Plasma Interactions 5: Inertial Confinement Fusion, page 105. (Proceedings of the 45th Scottish Universities Summer School in Physics, St Andrews, August 1994)* (Institute of Physics Publishing, 1995).

[11] T. Boehly, J. Delettrez, J. Knauer, D. Meyerhofer, B. Yaakobi, R. Town, and D. Hoarty, Physical Review Letters **87**, 145003 (2001).

[12] J. D. Kilkenny, S. G. Glendinning, S. W. Haan, B. A. Hammel, J. D. Lindl, D. Munro, B. A. Remington, S. V. Weber, J. P. Knauer, and C. P. Verdon, Physics Of Plasmas **1**, 1379 (1994).

[13] S. V. Weber, B. A. Remington, S. W. Haan, B. G. Wilson, and J. K. Nash, Physics Of Plasmas **1**, 3652 (1994).

[14] B. A. Remington, S. V. Weber, M. M. Marinak, S. W. Haan, J. D. Kilkenny, R. J. Wallace, and G. Dimonte, Physics Of Plasmas **2**, 241 (1995).

[15] T. Ma, N. Izumi, R. Tommasini, D. K. Bradley, P. Bell, C. J. Cerjan, S. Dixit, T. Doppner, O. Jones, J. L. Kline, et al., Review of Scientific Instruments **83**, 10E115 (2012).

[16] N. Izumi, T. Ma, M. Barrios, L. R. Benedetti, D. Callahan, C. Cerjan, J. Edwards, S. Glenn, S. Glenzer, J. Kilkenny, et al., Review of Scientific Instruments **83**, 10E121 (2012).

[17] A. G. MacPhee, D. H. Edgell, E. J. Bond, D. K. Bradley, C. G. Brown, S. R. Burns, J. R. Celeste, C. J. Cerjan, M. J. Eckart, V. Y. Glebov, et al., Journal of Instrumentation **6**, P02009 (2011).

[18] D. H. Edgell, D. K. Bradley, E. J. Bond, S. Burns, D. A. Callahan, J. Celeste, M. J. Eckart, V. Y. Glebov, D. S. Hey, G. LaCaille, et al., Review of Scientific Instruments **83**, 10E119 (2012).

[19] M. H. Key and R. J. Hutcheon, Advances in Atomic and Molecular Physics **16**, 201 (1980).

[20] F. J. Rogers, F. J. Swenson, and C. A. Iglesias, Astrophysical Journal v.456 **456**, 902 (1996).

[21] H. A. Scott and S. B. Hansen, High Energy Density Physics **6**, 39 (2010).

[22] V. Y. Glebov, T. C. Sangster, C. Stoeckl, J. P. Knauer, W. Theobald, K. L. Marshall, M. J. Shoup, T. Buczek, M. Cruz, T. Duffy, et al., Review of Scientific Instruments **81**, 10D325 (2010).

[23] D. L. Bleuel, C. B. Yeamans, L. A. Bernstein, R. M. Bionta, J. A. Caggiano, D. T. Casey, G. W. Cooper, O. B. Drury, J. A. Frenje, C. A. Hagmann, et al., Review of Scientific Instruments **83**, 10D313 (2012).

[24] D. T. Casey, J. A. Frenje, M. Gatu Johnson, F. H. Seguin, C. K. Li, R. D. Petrasso, V. Y. Glebov, J. Katz, J. P. Knauer, D. D. Meyerhofer, et al., Review of Scientific Instruments **83**, 10D912 (2012).

[25] P. Ross, J. Opt. Soc. Am **16**, 433 (1928).

[26] D. G. Hicks, N. B. Meezan, E. L. Dewald, A. J. Mackinnon, R. E. Olson, D. A. Callahan, T. Doppner, L. R. Benedetti, D. K. Bradley, P. M. Celliers, et al., Physics Of Plasmas **19**, 122702 (2012).

[27] D. A. Callahan, N. B. Meezan, S. H. Glenzer, A. J. Mackinnon, L. R. Benedetti, D. K. Bradley, J. R. Celeste, P. M. Celliers, S. N. Dixit, T. Doppner, et al., Physics Of Plasmas **19**, 6305 (2012).

[28] R. Betti, P. Y. Chang, B. K. Spears, K. S. Anderson, J. Edwards, M. Fatenejad, J. D. Lindl, R. L. Mccrory, R. Nora, and D. Shvarts, Physics Of Plasmas **17**, 058102 (2010).

[29] M. M. Marinak, G. D. Kerbel, N. A. Gentile, O. Jones, D. Munro, S. Pollaine, T. R. Dittrich, and S. W. Haan, Physics Of Plasmas **8**, 2275 (2001).

[30] D. S. Clark, D. E. Hinkel, D. C. Eder, O. S. Jones, S. W. Haan, B. A. Hammel, M. M. Marinak, J. L. Milovich, H. F. Robey, L. J. Suter, et al., Physics Of Plasmas (submitted, 2012).

[31] B. K. Spears, D. S. Clark, M. J. Edwards, S. W. Haan, J. D. Lindl, D. H. Munro, L. J. Suter, and C. A. Thomas, in *Bulletin of the American Physical Society* (2012), vol. 57, p. 112.

[32] R. H. H. Scott, D. S. Clark, D. K. Bradley, D. A. Callahan, M. J. Edwards, S. W. Haan, O. S. Jones, B. K. Spears, M. M. Marinak, R. P. J. Town, et al., Physical Review Letters (submitted, 2013).

[33] V. A. Thomas and R. J. Kares, Physical Review Letters **109**, 075004 (2012).

[34] B. A. Hammel, H. A. Scott, S. P. Regan, C. Cerjan, D. S. Clark, M. J. Edwards, R. Epstein, S. H. Glenzer, S. W. Haan, N. Izumi, et al., Physics Of Plasmas **18**, 056310 (2011).

[35] S. P. Regan, R. Epstein, B. A. Hammel, L. J. Suter, J. Ralph, H. Scott, M. A. Barrios, D. K. Bradley, D. A. Callahan, C. Cerjan, et al., Physics Of Plasmas **19**, 056307 (2012).